Inclusion-localised crystal-plasticity, dynamic porosity, and fast-diffusion pathway generation in zircon

Nicholas E. Timms[1]*, Steven M. Reddy[1], John D. Fitz Gerald[2], Leonard Green[3], and Janet R. Muhling[4]

1 Department of Applied Geology, Curtin University, GPO Box U1987, Perth, WA 6845, Australia

2 Research School of Earth Sciences, Australian National University, Canberra, 0200, Australia

3 Adelaide Microscopy, University of Adelaide, Adelaide, SA, 5005 Australia

4 Centre for Microscopy, Characterisation and Analysis, University of Western Australia, Perth, WA 6009, Australia

**Corresponding author. Email: n.timms@curtin.edu.au*

Keywords: zircon; electron backscatter diffraction; plastic strain; dislocation creep; diffusion; inclusion; pore

Abstract

A population of oscillatory zoned, igneous zircon grains in a Javanese andesite contains fluid and mineral inclusions (up to 10 μm across) trapped during zircon growth. Orientation contrast imaging and orientation mapping by electron backscatter diffraction reveal that crystal-plastic deformation overprints growth zoning and has localized around 1-10 μm pores and inclusions. Cumulative crystallographic misorientation of up to 25° around pores and inclusions in zircon is predominantly accommodated by low-angle (<5°) orientation boundaries, with few free dislocations in subgrain interiors. Low-angle boundaries are curved, with multiple orientation segments at the sub-micrometer scale. Misorientation axes associated with the most common boundaries align with the zircon *c*-axis and are consistent with dislocation creep dominated by <100>(010) slip. A distinctly different population of sub-micron pores is present along subgrain boundaries and their triple junctions. These are interpreted to have formed as a geometric consequence of dislocation interaction during crystal plasticity. Dislocation creep microstructures are spatially related to differences in cathodoluminescence spectra that indicate variations in the abundance of CL-active rare earth elements. The extent of the modification suggests deformation-related fast-pathway diffusion distances that are over five orders of magnitude greater than expected for volume diffusion. This enhanced diffusion is interpreted to represent a combination of fast-diffusion pathways associated with creep cavitation, dislocations and along low-angle boundaries. The implication of these new data is that ductile deformation localised around inclusions can provide fast pathways for geochemical exchange links to external phases and thus negate the widely held assumption that inclusions in fracture-free zircon are always geochemically armoured once they are physically enclosed.

Introduction

The growth of zircon ($ZrSiO_4$) from a melt or in metamorphic rocks is commonly accompanied by entrapment or overgrowth of solid mineral phases, melt or fluid inclusions at the migrating zircon/matrix interface. Zircon from a wide range of igneous rock types contains inclusions, that have been used to reveal information about the magma composition from which the zircon grew, temperature conditions during zircon growth, and melt/zircon partition coefficients (Chupin et al. 1998, Danyushevsky et al. 2002, Li 1994, Thomas et al. 2003, Thomas et al. 2002). The integration of petrological and geochemical studies of the inclusion mineralogy with U-Pb geochronology and trace element geochemistry of zircon permits petrogenetic processes to be placed within an absolute temporal framework. Such an approach can be valuable, for example, in constraining prograde metamorphic pressure-temperature-time paths that are otherwise difficult or impossible to access (Katayama & Maruyama 2009, Katayama et al. 2002, Liu et al. 2004, Massonne & Nasdala 2003). Significantly, the ability of zircon to resist chemical and physical breakdown allows old zircons to be used to constrain processes in the early Earth, for example to support the presence of volatile-rich granitoid magmas in the Archaean (Chupin et al. 1998), cool Hadean surface temperatures (Hopkins et al. 2010), and the operation of subduction as far back as 4.25 Ga (Menneken et al. 2007, Nemchin et al. 2008).

Critical to the application of mineral and/or fluid inclusions (pores) in zircon to petrogenetic processes is the assumption that the inclusions have been armoured by the zircon and have remained isolated from chemical exchange. Several processes are known to cause the formation of secondary mineral phases and pores in zircon. Hydrothermal alteration of zircon results in migration of reaction interfaces through grains, leaving recrystallised zircon and newly developed pores in their wake (Geisler et al. 2001, Geisler et al. 2003). Extreme conditions associated with impacts can lead to phase transformations and decomposition of zircon (Glass et al. 2001, Wittmann et al.

2006). At high shock pressures (>30GPa), zircon can form microtwins (Leroux et al. 1999, Timms et al. in press) and contain traces of high pressure polymorph reidite, most commonly as fine-scale epitaxial lamellae (Glass et al. 2001, Leroux et al. 1999). Zircon can also form a granular structure with 'microvesicles' during impact events, and decomposes to baddeleyite and other ZrO_2 polymorphs (Buttermann & Foster 1967, Wittmann et al. 2006).

The studies of zircon inclusions often assume that the inclusions are chemically isolated from the rock matrix by the armoring characteristics of the zircon host. The justification of this assumption arises from the low diffusivity for volume diffusion of major and trace elements in zircon at crustal temperatures (<900º C) over geological timescales (Cherniak & Watson 2003). However, numerous studies have demonstrated that fractures that link the inclusion to the zircon rim allow geochemical exchange between inclusion and rock matrix (e.g., Qin 1992). Inclusions affected in this way can usually be identified since fractures are readily observable by most zircon imaging techniques and can be routinely avoided. More subtle microstructures identified by electron backscatter diffraction and associated with crystal-plastic deformation of zircon have recently been discovered in a range of geological environments (Kaczmarek et al. in press, Moser et al. 2009, Nemchin et al. 2009, Reddy et al. 2009, Reddy et al. 2006, Timms et al. 2006, Timms et al. in press)}. These microstructures, commonly low-angle boundaries formed by the interaction of dislocations during dislocation creep (Reddy et al. 2007), have been shown to facilitate chemical and isotopic exchange between the zircon and the rock matrix (Moser et al. 2009, Nemchin et al. 2009, Reddy et al. 2006, Timms et al. 2006, Timms et al. 2011, Timms & Reddy 2009) by providing fast diffusion pathways that increase the bulk diffusivity of the zircon at the grain-scale. Closer examination of deformed igneous zircon grains from a Javanese andesite previously described by Reddy et al. (2009) has revealed that the grains contain fluid and solid mineral inclusions. In this paper, we examine the relationships between zircon deformation, recorded by the spatial development of crystal-plastic

93 microstructures, ‘pores’ and included mineral phases. We provide the first evidence that primary
94 inclusions can localize crystal-plastic deformation in zircon, and demonstrate for the first time that
95 this deformation can be accompanied by the development of new porosity. We confirm that
96 microstructural networks that surround inclusions are fast pathways for trace element exchange.
97 These observations provide the first examples of alternative pathways for fast diffusion coupling
98 between inclusion and rock matrix that may sometimes breach the assumption of chemical isolation
99 of inclusion phases.
100
101 **Sample Description**
102 The zircon grains used in this study have been described previously (Reddy et al. 2009) and are
103 from an undeformed glomeroporphyritic andesite (Jhs2Pon4) from the boundary between the
104 Southern Mountains Arc and the active Sunda Arc of the Ponorongo region of East Java, Indonesia
105 (7º50’28.8”S; 111 º 19’45.6”E) (Smyth et al. 2007). The studied rock contains two distinct
106 populations of zircon. One population of zircon grains is undeformed, shows a wide variety of
107 colours (colourless, yellow, brown) and sizes (100-300 μm long) and shapes (rounded to subhedral),
108 records a range of Archaean to Cambrian ages and is interpreted to be xenocrystic (Reddy et al.
109 2009). The grains of the second population are 150-500 μm long, euhedral orange crystals, which
110 show complex oscillatory zones in cathodoluminescence images (Fig. 1) and preserve uniform U-
111 Pb ages with a mean age of 9.28 ± 0.21 Ma (Reddy et al. 2009). These grains are interpreted to be
112 ‘magmatic’ and petrogenetically related to the andesite (Reddy et al. 2009). Approximately 80% of
113 the magmatic grains preserve crystal-plastic deformation microstructures and spatially-associated
114 disrupted cathodoluminescence properties (Reddy et al. 2009, Timms & Reddy 2009). These
115 deformation microstructures are best seen in orientation contrast images (OCI), electron backscatter
116 diffraction (EBSD) and hyperspectral cathodoluminescence (CL) maps, yet are cryptic in
117 panchromatic CL images and not apparent via optical microscopy (Timms & Reddy 2009). The

deformation of these zircon grains is interpreted to have taken place within a low-melt fraction adcumulate stage of a crystallizing magma in the mid- to lower crust (Reddy et al. 2009). Disaggregation of this cumulate and remobilization by a second melt phase resulted in melt migration through the crust, xenocryst scavenging and emplacement of the andesite at shallow crustal levels. This study examines porosity and inclusion-related microstructures within this younger population of zircon grains.

Analytical Techniques

The separation of zircon from the sample, and details of the mounting and polishing procedures and cathodoluminescence imaging have been presented in detail elsewhere in Reddy et al. (2009). Orientation contrast imaging was performed on polished sections of the grains as a rapid means of providing qualitative microstructural information (e.g., Lloyd 1987), and were acquired using a Zeiss Neon 40 dual beam focused ion beam (FIB) field emission gun (FEG) SEM at Curtin University. Orientation contrast was achieved on untilted samples using an annular backscattered electron detector and reduction of the working distance to ~5 mm, and, thus increasing the effective take-off angle of backscattered electrons. This technique is an alternative to the forward-mounted detectors used for simultaneous OCI and EBSD mapping, (e.g., Prior et al. 1999), that overcomes problematic shadow effects from detection from a limited range of angles.

Quantitative microstructural data were collected via EBSD mapping undertaken on a Phillips XL30 FEG SEM fitted with an Oxford Instruments EBSD acquisition system, based at Adelaide Microscopy, University of Adelaide, South Australia. SEM and EBSD settings were optimized for zircon after Reddy et al. (2007) and Reddy et al. (2008), and are given with EBSD indexing statistics in Table 1. All EBSD data were processed using Oxford Instruments Channel 5 (SP9) software using procedures detailed elsewhere (Reddy et al. 2007). EBSD data were used to

142 generate orientation maps, crystallographic pole figures and misorientation axis distributions.
143 Details of these plotting procedures have also been described elsewhere (Reddy et al. 2007).
144 Focussed ion beam milling was used to prepare samples for transmission electron
145 microscopy (TEM) and provided an assessment of the microstructural geometry in three
146 dimensions. FIB-milling was done using an FEI Helios DualBeam FIB-SEM D433 at Adelaide
147 Microscopy, University of Adelaide, using settings given in Table 1. The FIB-milling procedure
148 involved deposition of a protective platinum strip (2 μm wide x 1 μm deep), then 'rough' milling a
149 rectangular trench at 30 kV and 21 nA probe current, and 9.3 / 2.8 nA to reduce milling artefacts.
150 The vertical trench wall was then given a 'fine' mill at 30 kV and 9.3 nA to reduce ion damage and
151 secondary deposition. Secondary electron images were taken using an electron beam at 20 kV and
152 21 pA / 0.17 nA current. TEM foils were prepared following the same procedure but with a wedge
153 cut symmetrically either side of the platinum strip. The region of interest was then milled from the
154 sample (30 kV beam and 2.8 nA current), picked up and welded (30 kV beam and 9.7 nA current)
155 to an Omniprobe TEM grid within the SEM via a micro-manipulator, and thinned to ~500 nm on
156 both sides using a 2.8 nA beam, then further using a 48 pA beam. The foil surfaces were 'cleaned'
157 using 5 kV, 16 pA beam at ± 8° tilt for 5 minutes each.
158 TEM imaging and diffraction was conducted using a Philips CM300T instrument at the
159 Australian National University in Canberra. The instrument was operated at 300 kV and images
160 recorded via a Gatan MSC 794 digital camera. The FIB-prepared foils were manipulated in the
161 TEM using a conventional double-tilt specimen holder.
162 Hyperspectral cathodoluminescence data were collected using a 2049-element linear
163 spectrometer / CCD-Si mounted on a JEOL 8530F FEG electron microprobe in the Centre for
164 Microscopy, Characterisation and Analysis at the University of Western Australia, Perth. Probe
165 conditions were optimized for spatial resolution with 10 kV accelerating voltage and 10 nA probe
166 current. Spatial resolution at these conditions is approximately 1 μm. Automated mapping involved

167 the collection of CL spectra in 196-903 nm wavelength range on a user defined grid with node
168 spacing of 300 nm. Dwell times per point of 800 ms were used to achieve an acceptable signal to
169 noise ratio. Hyperspectral CL data were processed using xCLent III software (MacRae et al. 2005).
170 Trichromatic maps were produced by assignment of three colour channels to wavelength ranges that
171 define the dominant peaks in CL emission. Mean CL spectra for regions of interest on the map are
172 presented as raw counts and normalized to a spectrum from the zircon core for the purpose of
173 comparison.
174
175 **Results**
176 Orientation contrast imaging shows that over 75% of the zircon grains from the 9.3 Ma population
177 contain lattice orientation variations that occur throughout the grains and are not limited to just
178 grain edges (Fig. 2). In all cases, orientation variations are most commonly manifest by discrete,
179 polygonal boundaries, with relatively few domains of gradational change. These deformation
180 microstructures cross cut primary growth zones seen in CL images (Figs 1, 2). Orientation
181 boundaries and, more commonly, their triple junctions are decorated with type 2 pores. Orientation
182 domains are commonly curved, yet; the trace of the boundaries visible on the prepared surface of
183 the zircon are predominantly aligned parallel to the c-axis of the grains (Fig. 2b, c).
184
185 Pores occur throughout all of the 9.3 Ma igneous zircon grains, and form two distinct groups based
186 on their size and shape characteristics. The larger pores (type 1 pores) are approximately 1 to 7 μm
187 across, have irregular cuspate shapes with concave walls, and occur in the oscillatory-zoned rims of
188 the grains. (Figs 2, 3). Magnetite (Fe_3O_4) inclusions, typically 1-3 μm across, are sometimes found
189 within type 1 pores (Figs 2e, 4b). Smaller pores (type 2 pores) are much more numerous (>80% by
190 frequency), are typically 100-400 nm across, have simple shapes with low aspect ratios, and
191 typically occur in clusters and trails in the vicinity of larger pores (Figs 2, 3). Like the larger pores,

192 these cavities have cuspate margins with pointed edges and terminations. 3D analysis of the pore
193 space (Fig. 2c-d) by focussed ion beam milling shows that type 1 and type 2 pores extend beneath
194 the sample surface and are not formed by the plucking out of material during polishing. There is no
195 evidence of melt in the magnetite inclusions or pores.
196
197 EBSD orientation maps show changes in lattice orientation across the grain accommodated by
198 orientation boundaries with 1-20° misorientations, or 'low-angle boundaries' (Figs 4, 5) with the
199 most complex and intensely developed microstructures being proximal to the type 1 pores and
200 mineral inclusions. Low-angle boundaries delimit domains with little orientation variation, or
201 'subgrains' (Reddy et al. 2009). Grain 5 contains a complex, irregular type 1 pore that also contains
202 a microcrystal of magnetite. The magnetite has curved interfaces with the pore and host zircon, and
203 preserves intragrain crystallographic misorientation of up to 5° accommodated by a low-angle
204 boundary (Fig. 4b). The magnetite-pore 'inclusion' is surrounded by low-angle boundaries that
205 define an ellipsoidal zone of subgrains around the microcrystal of magnetite (Fig. 4b). The long axis
206 defined by the network of subgrains is within 10° of the c-axis of the grain. The network of low-
207 angle boundaries link pores and inclusions with the grain boundary of the zircon (Figs 2 and 4).
208
209 EBSD data show the dispersion of lattice orientations (Fig. 4c-d) and the majority of low-angle
210 misorientation axes (Fig. 5) are sub-parallel to <c> of the zircon grain. Some low-angle boundaries
211 have misorientation axes that lie parallel to the *a*-planes or coincide with other low-index
212 crystallographic directions (Fig. 5). These boundaries are interspersed throughout the deformation
213 microstructure, and do not show systematic relationships with strain intensity or position relative to
214 pores (Fig. 5).
215

TEM foils were made across boundaries with different boundary plane - misorientation axis relationships to determine the nature of the slip systems in different boundary geometries (Fig. 6a). TEM analysis shows that all of the lattice misorientation in these domains occurs at the boundaries with almost no free dislocations within subgrains (Fig. 6). Black spots visible in the TEM images represent nano-sized regions where the crystal has some local point imperfection resulting in a small surrounding zone of elastic lattice strain. These regions diffract differently to the surrounding unstrained crystal, hence they appear darker in these brightfield TEM images. The nature of the imperfections was not established and they may have more than one origin. Their likely causes include nano-sized inclusions, centres of natural radiation damage or artefacts of FIB milling.

A low-angle (~1.4°) boundary shows strain indicating that it is accommodated by necessary dislocations (Fig. 6d). This boundary has local variations in orientation and is approximately parallel to (110). A boundary with 3.5 ° misorientation around <c> also has local variation in the orientation of the boundary plane at the TEM scale, and locally parallel with (011) and (001) (Fig. 6f, g). Periodic contrast (ledges?) can be seen along the boundary at around 20 nm spacing and are inconsistent with a perfect twist boundary of [100] + [010] screw dislocations with [001] twist axis and Burgers' vector magnitude of 6 Å because dislocations in each set would be spaced apart by ~10 nm for a 3.5° misorientation through geometric necessity (Fig. 6f, g).

A boundary with ~4˚ misorientation around <c> shows periodic contrast at 10-15 nm scale, no free dislocations, has a variable boundary orientation and is faceted at the 100-250 nm scale (Fig. 6e). Here the longest facets lie near (010) and could be arrays of edge dislocations with [010] Burgers' vector and slip plane (100), as such could be pure tilt segments. However, the intervening facets are not well defined and the majority of the boundary is not of this type. A boundary with 16˚ misorientation around <c> is curved and has no sign of dislocation contrast (Fig. 6d).

Hyperspectral CL mapping shows that the oscillatory growth zoning pattern in the rim and the relatively homogeneous core zones are superimposed by networks of bands and patchy domains with significantly different CL characteristics to the host zircon, seen as orange-yellow areas on Fig. 7a. These CL patterns spatially coincide with the low-angle boundary and subgrain microstructures identified by orientation contrast imaging and EBSD mapping (Figs 2-5). Significantly, these microstructures cross cut primary growth zoning in the core and oscillatory zoned rim, and connect type 1 pores with the zircon grain boundary (Fig. 7a). Analysis of the CL spectra shows three dominant broad peaks at ~400, ~475 and ~525 nm, with narrow peaks superimposed at many different wavelengths (Fig. 7b). Normalization of spectra from different parts of the zircon to that of the homogeneous core permits a comparison of the intensity of the emission wavelengths relative to the core (Fig. 7c). The brighter parts of the oscillatory zoned rim has relatively more intense luminescence in 315-460 nm range with peaks at 350, 380 and 405 nm, and relatively less luminescence in the 460-680 nm range with troughs at 470, 520 and 570 nm (Fig. 7c). The spectrum from the darker unaltered banded area has lower CL signal, and lower peaks in the 350-780 nm range relative to the core (Fig. 7c). Spectra from the darker banded domains have more similarities in shape to the bright parts of the rim (area 1 in Fig. 7) than the core (area 4 in Fig. 7). Poor signal in these low-luminescent areas has resulted in significantly lower signal to noise ratio than in normalised spectra from strongly luminescent areas (Fig. 7c). Spectra from two 'altered' domains show a different pattern from the core and rim spectra and have relatively less emission in the 315-485 nm range with troughs at ~345, 382, 405 and 470, and relatively stronger emission from 485-700 nm with peaks at 512, 548, 559 and ~587 nm (Fig. 7c).

Discussion

Deformation mechanism of zircon

266 The development of low-angle boundaries, subgrains, and progressive changes in crystallographic
267 orientation with rational, low-index misorientation axes is consistent with deformation by the
268 formation and migration of dislocations. The predominance of low-angle boundaries suggests that
269 dislocation glide and climb were operational to accumulate dislocations into subgrain boundaries
270 whilst leaving the subgrain interiors without free geometrically necessary dislocations. Such
271 dislocation creep microstructures are usually indicative of high temperature creep in other minerals
272 (e.g., Hirth & Tullis 1992). Zircon deformation took place due to tectonic stresses within a low-melt
273 fraction (\5% melt), mid-lower crustal cumulate prior to magmatic disaggregation and ascent to
274 higher crustal levels in the Sunda Arc (Reddy et al. 2009). The trend of crystallographic
275 misorientation axes associated with low-angle boundaries and the trace of the low-angle boundary
276 on the sample surface can be used to determine the dominant dislocation slip system responsible for
277 the low-angle boundary by using simple geometric models (Boyle et al. 1998, Prior et al. 2002,
278 Reddy et al. 2007). The data are consistent with 'tilt' and 'twist' boundaries, where the
279 misorientation axes are parallel with and perpendicular to the low-angle boundary surfaces,
280 respectively. The majority of the low-angle boundaries have misorientation axes that cluster at or
281 near the zircon c-axis direction (Fig. 5c-d). The variable orientation of these boundaries suggests
282 that their formation is dominated by the accumulation of varying combinations of either screw
283 and/or edge dislocations, including dislocations with one of the two symmetrically equivalent
284 <100> Burgers vectors. This supports findings from other studies that indicate that the <100>{010}
285 slip system is common in crystal-plastically deformed zircon (Leroux et al. 1999, Moser et al. 2009,
286 Nemchin et al. 2009, Reddy et al. 2009, Reddy et al. 2007, Timms et al. 2006, Timms et al. 2011).
287 The small number of low-angle boundaries with non-c-axis-parallel misorientation axes are a
288 consequence of various degrees of mixing between <100>{010} and <001>{100} slip, and/or the
289 activity of higher order slip systems. Very few of the boundaries seen with TEM in the FIB foils
290 have pure tilt or twist character. In fact, the variation of angle between misorientation axis and

boundary-plane normal by over 90° for most low-angle boundaries indicates an overall lack of either dominant tilt or twist geometries (Fig. 5c, d).

Origin of type 1 pores and inclusions

It has been demonstrated that brittle fracture can precede and facilitate ductile deformation (and eventually recrystallisation at higher strains) of quartz, feldspar and olivine (Cordier & Doukhan 1989, Gerald et al. 1991, Green II & Gueguen 1983, Stünitz et al. 2003, Trepmann & Stöckhert 2003, Vernooij et al. 2006). In these studies, dilatation and healing of fractures led to the development of trains of fluid inclusions with cuspate boundaries along the traces of fracture planes. In this study the type 1 pores show no evidence of fracture-related crystallographic misorientation or systematic trains of inclusions, such as would be expected at dilatational jogs along stepped or intersecting fracture planes, newly grown (healed) zircon or fracture traces in CL images. It is therefore unlikely that type 1 pores represent secondary fluid inclusions associated with healed fractures. The clustering and intimate relationship between type 1 pores and mineral inclusions along similar growth zones indicates that type 1 pores represent 'primary' fluid inclusions trapped during the crystallization of zircon from melt. Therefore, type 1 pores are trapped bubbles of a co-magmatic fluid phase, such as CO_2, H_2O or CH_4-rich fluids, and inclusions of microcrystalline magnetite.

Dynamic generation of type 2 porosity by 'creep cavitation'

The type 2 pores lie at the triple junctions of the subgrain boundaries and, less commonly, along low-angle boundaries (Fig. 2b, c). The occurrence of sub-micron pores at subgrain boundary triple junctions and boundaries (e.g., Fig. 2b, c) is strong evidence of cavitation caused during dislocation creep in zircon (Fig. 8). It is has been proposed that during dislocation creep, nanometer-scale cavities, known as Zener-Stroh cracks, accumulate at grain boundaries and triple junctions by

316 dislocation pile-ups (Stroh 1957, Weertman 1986). Weertman (1986) suggested that two or more
317 edge dislocations sliding on a single plane could coalesce into a newly opened space (effectively a
318 nano-size crack) so that then becomes the nucleus of a Zener-Stroh macro-crack. As such, tubule-
319 shaped cavities tend to form parallel to dislocation lines at low-angle boundaries. The cavities at
320 triple junctions can be caused by the coalescence of dislocations pile-ups on more than one
321 intersecting slip plane (Cottrell, 1958). Cavitation of high-angle grain boundary triple junctions is
322 usually a sign of grain-boundary sliding. However, this deformation mechanism is unlikely because
323 the triple junctions are for low-angle boundaries and the bulk strain in the grains is clearly very
324 small. Vacancy agglomeration could also contribute to cavitation at boundaries (Raj & Ashby
325 1975). This mechanism of void growth involves the condensation of vacancies along boundaries via
326 diffusion, a process that becomes more important with increasing temperature conditions (Kassner
327 & Hayes 2003). The size of Zener-Stroh cavities is a function of the local low-angle boundary
328 orientations, the dislocation slip systems that contributed to their development, and the total
329 misorientation in the vicinity of the triple junction (Dyson 1983, Westwood et al. 2004). However,
330 type 1 pores do not show a relationship between the magnitude of local misorientation or boundary
331 geometry with pore size (Fig. 5), and are inconsistent with a creep cavitation origin, which is in
332 agreement with a primary inclusion origin for type 1 pores.
333
334 ***The relationship of type 1 pores and mineral inclusions with the deformation microstructure***
335 Type 1 pores and mineral inclusions are surrounded by crystal-plastic microstructures, recognized
336 by EBSD mapping. It has been demonstrated that dislocation-related defects, such as low-angle
337 boundaries, can nucleate at irregularities on crystal interfaces, such as inclusions, and propagate
338 during mineral growth (Bestmann et al. 2005, Timms et al. 2009). The distribution of defects
339 around type 1 pores and mineral inclusions is relatively symmetric (prolate) and not related to the
340 direction of crystal growth. This eliminates the possibility that the crystal defects nucleated at the

341 zircon-inclusion interface during growth. Furthermore, the deformation microstructures cross cut
342 growth zoning in the cores and rims. Therefore, the microstructures must have localised around the
343 type 1 pores and mineral inclusions after the zircon had grown. This is supported by the fact that the
344 magnetite grain also preserves crystal-plastic deformation microstructures (Fig. 4b).
345
346 The nature of the interaction between localised inclusion-related stress and the anisotropic
347 properties of zircon are unknown. However, the pseudo-elliptical (ellipsoidal in 3D?) pattern of
348 plastic strain around the magnetite inclusion may represent the ductile response to localised stress
349 perturbations with a similar geometry to that of the enveloping elastic field developed around a pre-
350 existing inclusion (Eshelby 1959, Healy 2009, Nasdala et al. 2005). The patterns of deformation
351 microstructures around inclusions also have some similarities to those observed around mineral
352 inclusions in diamonds that result from stresses that arise from relative volume changes during
353 exhumation from the lower mantle (Cayzer et al. 2008). However, in this study deformation-related
354 microstructures are prevalent away from inclusions, indicating that tectonic stresses were sufficient
355 for zircon deformation without requiring stresses associated with volume changes (Reddy et al.
356 2009). The data presented here show that the presence of type 1 pores and mineral inclusions in
357 zircon can localize crystal-plastic deformation within the interior of grains and not necessarily just
358 at the edge of grains.
359
360 The minimization of surface energy during entrapment of primary fluid inclusions would have
361 resulted in simple sub-spherical pore geometries (e.g., Corfu et al. 2003, Thomas et al. 2003)(Fig.
362 8). Therefore, the complex concave walls of the large pores (e.g., Fig. 2b, e) suggest that the zircon-
363 pore interfaces have been modified (Fig. 8). It is plausible that the type 1 pores have undergone
364 limited shape modification by Zener-Stroh mechanisms. However, the highly irregular type 1 pore
365 shapes require other deformation mechanisms, such as mass transfer accommodated boundary

366 migration, or surface energy driven grain boundary bulging of zircon into the pore spaces. These
367 processes require that either the pore-filling phase was compressible or has 'leaked' from the pores
368 during deformation. If the latter is true, then the relatively disordered structure and Zener-Stroh
369 cavities of low-angle boundaries are the most likely pathways for leakage from pores in the grains.
370
371 ***The relationship between rare earth element composition and deformation microstructure***
372 Hyperspectral CL mapping shows a link between the deformation microstructure and altered CL
373 response (Fig. 7). It is well established that the main cause of cathodoluminescence of zircon is the
374 incorporation of trivalent rare earth elements (REE^{3+}) into the zircon structure (Blanc 2000,
375 Cesbron et al. 1995, Nasdala et al. 2002, Nasdala et al. 2003, Remond et al. 1992). Individual
376 REE^{3+}s cause emission over several specific narrow wavelength ranges, or 'bands', commonly with
377 one or two dominant bands (Blanc 2000, Gaft et al. 2000). The sum of all emission bands gives the
378 shape of the CL spectra and the integrated intensity seen in panchromatic CL images (Fig. 1).
379 Therefore, the CL spectra from grain 8 can be interpreted in terms of contributions of luminescence
380 from a variety of REE^{3+}, the dominant peaks of which are annotated on Fig. 7c. In studies where
381 REE concentrations have been measured by ion microprobe, CL peak intensity generally
382 corresponds to REE concentration in deformed zircon (e.g., Reddy et al. 2006). However, the
383 microstructures and associated alteration domains in this example are much finer than the diameter
384 of an ion microprobe analysis spot (SHRIMP = 20 μm), and preclude ion microprobe calibration of
385 the hyperspectral CL data due to problems associated with volume averaging in the analytical spot.
386 Furthermore, overlaps of minor peaks from different REE^{3+} and poorly understood effects of other
387 defects (e.g., OH^- defects and radiation damage) negate reliable deconvolution of hyperspectral CL
388 data for REE^{3+}. Nevertheless, dominant peaks observed in the normalized CL spectra correspond
389 closely with REE^{3+} peaks. Changes in the relative peak intensities are interpreted to be related to
390 changes in the relative concentration of different REE^{3+} such that light to middle REE (Pr, Sm, Eu)

391 are relatively enriched over middle to heavy REE (Tm, Er, Dy, Tb) in the vicinity of low-angle
392 boundaries (Fig. 7b). This is consistent with the links between crystal-plasticity, CL and REE in
393 zircon reported elsewhere (Reddy et al. 2006, Timms et al. 2011, Timms & Reddy 2009), and
394 implies open system REE exchange between zircon and an external source.
395
396 ***Fast pathways for element exchange during ductile deformation in zircon***
397 The crystallization U-Pb age of 9.28 ± 0.21 Ma for the population of zircon grains obtained by
398 Reddy et al. (2009) places upper bounds for the temperature-time history of these grains. The grains
399 must have remained closed to Pb diffusion since their crystallization, and so cannot have been
400 above ~800-850°C (Cherniak & Watson 2003). Simple modeling for these temperature and time
401 conditions shows that the distances over which REE modification is observed in these grains (~50
402 μm) is at least five orders of magnitude more than that expected for volume diffusion (assuming a
403 spherical geometry and diffusion parameters of Cherniak et al. (1997). Therefore, this study
404 identifies that dislocations and low-angle boundaries, spatially associated with inclusions, provide
405 fast diffusion pathways that link inclusions to the grain boundary network. Furthermore, dynamic
406 development of new porosity along low-angle boundaries by dislocation creep cavitation represents
407 a previously unrecognized type of fast-diffusion pathway in zircon. So-called 'creep cavitation' has
408 been identified as a potentially important mechanism for the generation of permeable pathways in
409 metamorphic rocks (Delle Piane et al. 2009, Fusseis et al. 2009, Mancktelow et al. 1998, Rybacki et
410 al. 2008). Crystal plastic deformation around inclusions may therefore facilitate modification of
411 inclusion chemistry, thereby negating the assumption of inclusion armouring by the host zircon.
412 The presence of pre-existing pores and inclusions can locally enhance plastic deformation because
413 they are stress risers within zircon, and could localize plastic strain of the surrounding zircon. Fluids
414 from within pores could facilitate mass transfer along deformation-related defects in zircon.
415
416

Acknowledgements

Rob Hart (Applied Physics, Curtin University) is thanked for assistance with electron microscopy. The facilities of the Australian Microscopy & Microanalysis Research Facility (AMMRF) at the Centre for Microscopy, Characterisation & Analysis (UWA) and Adelaide Microscopy (University of Adelaide) are funded by the Universities, State and Commonwealth Governments. This research was supported by Australian Research Council Discovery Project DP0664078 and an AMMRF TAP grant. S. Reddy acknowledges a Curtin University Targeted Research Fellowship. We acknowledge Lutz Nasdala, Yves Gueguen, Nicola Cayzer, Charles Onasch and two anonymous reviewers for their constructive reviews of earlier versions of the manuscript. This is TIGeR publication number XXX.

References

Bestmann, M., Piazolo, S., Spiers, C. J. & Prior, D. J. 2005. Microstructural evolution during initial stages of static recovery and recrystallization; new insights from in-situ heating experiments combined with electron backscatter diffraction analysis. *Journal of Structural Geology* **27**(3), 447-457.

Blanc, P., Baumer, A, Cesbron, F, Ohnenstetter, D, Panczer, G, Rémond, G. 2000. Systematic Cathodoluminescence Spectral Analysis of Synthetic Doped Minerals: Anhydrite, Apatite, Calcite, Fluorite, Scheelite and Zircon. In: *Cathodoluminescence in Geosciences* (edited by Pagel, M., Barbin, V., Blanc, P. & Ohnenstetter, D.). Springer-Verlag, Berlin, 127-160.

Boyle, A. P., Prior, D. J., Banham, M. H. & Timms, N. E. 1998. Plastic deformatrion of metamorphic pyrite: new evidence from electron backscatter diffraction and forescatter orientation-contrast imaging. *Mineralium Deposita* **34**, 71-81.

Buttermann, W. C. & Foster, W. R. 1967. Zircon stability and the ZrO 2 -SiO 2 phase diagram. *American Mineralogist* **52**, 880-885.

442 Cayzer, N. J., Odake, S., Harte, B. & Kagi, H. 2008. Plastic deformation of lower mantle diamonds
443 by inclusion phase transformations. *Eur J Mineral* **20**(3), 333-339.
444 Cesbron, F., Blanc, P., Ohnenstetter, D. & Rémond, G. 1995. Cathodoluminescence of rare earth
445 doped zircons: I. Their possible use as reference materials. *Scanning Microscopy*
446 *Supplement* **9**, 35-56.
447 Cherniak, D. J., Hanchar, J. M. & E.B., W. 1997. Rare-earth diffusion in zircon. *Chemical Geology*
448 **134**, 289-301.
449 Cherniak, D. J. & Watson, E. B. 2003. Diffusion in zircon. In: *Reviews in Mineralogy and*
450 *Geochemistry: Zircon* (edited by Hanchar, J. M. & Hoskin, P. W. O.). *Reviews in*
451 *Mineralogy and Geochemistry, v. 53* **53**. Mineralogical Society of America, 113-143.
452 Chupin, S. V., Chupin, V. P., Barton, J. M. & Barton, E. S. 1998. Archean melt inclusions in zircon
453 from quartzite and granitic orthogneiss from South Africa; magma compositions and
454 probable sources of protoliths. *Eur J Mineral* **10**(6), 1241-1251.
455 Cordier, P. & Doukhan, J. C. 1989. Water solubility in quartz and its influence on ductility. *Eur J*
456 *Mineral* **1**(2), 221-237.
457 Corfu, F., Hanchar, J. M., Hoskin, P. W. O. & Kinny, P. 2003. Atlas of Zircon Textures. In:
458 *Reviews in Mineralogy and Geochemistry: Zircon* (edited by Hanchar, J. M. & Hoskin, P.
459 W. O.) **53**. Mineralogical Society of America, 469-500.
460 Cottrell., A. H. 1958. *Transactions Metallurgy Society AIME* **212**, 192-203.
461 Danyushevsky, L. V., McNeill, A. W. & Sobolev, A. V. 2002. Experimental and petrological
462 studies of melt inclusions in phenocrysts from mantle-derived magmas: an overview of
463 techniques, advantages and complications. *Chemical Geology* **183**(1-4), 5-24.
464 Delle Piane, C., Wilson, C. J. L. & Burlini, L. 2009. Dilatant plasticity in high-strain experiments
465 on calcite-muscovite aggregates. *Journal of Structural Geology* **31**(10), 1084-1099.

466 Dyson, B. F. 1983. Continuous cavity nucleation and creep fracture. *Scripta Metallurgica* **17**(1), 31-
467 37.
468 Eshelby, J. D. 1959. The elastic field outside an ellipsoidal inclusion, and related problems. *Proc.*
469 *Roy. Soc. London* **A252**, 561-569.
470 Fusseis, F., Regenauer-Lieb, K., Liu, J., Hough, R. M. & De Carlo, F. 2009. Creep cavitation can
471 establish a dynamic granular fluid pump in ductile shear zones. *Nature* **459**(7249), 974-977.
472 Gaft, M., Panczer, G., Reisfeld, R. & Shinno, I. 2000. Laser-induced luminescence of rare-earth
473 elements in natural zircon. *Journal of Alloys and Compounds* **300-301**, 267-274.
474 Geisler, T., Ulonska, M., Schleicher, H., Pidgeon, R. T. & van Bronswijk, W. 2001. Leaching and
475 differential recrystallization of metamict zircon under experimental hydrothermal
476 conditions. *Contributions to Mineralogy and Petrology* **141**(1), 53-65.
477 Geisler, T., Zhang, M. & Salje, E. K. H. 2003. Recrystallization of almost fully amorphous zircon
478 under hydrothermal conditions: An infrared spectroscopic study. *Journal of Nuclear*
479 *Materials* **320**(3), 280-291.
480 Gerald, J. D. F., Boland, J. N., McLaren, A. C., Ord, A. & Hobbs, B. E. 1991. Microstructures in
481 Water-Weakened Single Crystals of Quartz. *J. Geophys. Res.* **96**(B2), 2139-2155.
482 Glass, B. P., Liu, S., Glass, B. P. & Fries, M. 2001. Discovery of high-pressure ZrSiO4 polymorph
483 in naturally occurring shock-metamorphosed zircons: Micro-Raman spectroscopic study of
484 fine-grained, shock-metamorphosed rock fragments from the Australasian microtektite
485 layer. *Geology* **29**(4), 371-a-373.
486 Green II, H. W. & Gueguen, Y. 1983. Deformation of peridotite in the mantle and extraction by
487 kimberlite: A case history documented by fluid and solid precipitates in olivine.
488 *Tectonophysics* **92**(1-3), 71-92.
489 Healy, D. 2009. Elastic field in 3D due to a spheroidal inclusion--MATLAB(TM) code for
490 Eshelby's solution. *Computers & Geosciences* **35**(10), 2170-2173.

491 Hirth, G. & Tullis, J. 1992. Dislocation creep regimes in quartz aggregates. *Journal of Structural*
492 *Geology* **14**(2), 145-159.
493 Hopkins, M. D., Harrison, T. M. & Manning, C. E. 2010. Constraints on Hadean geodynamics from
494 mineral inclusions in > 4 Ga zircons. *Earth and Planetary Science Letters* **298**(3-4), 367-
495 376.
496 Kaczmarek, M. A., Reddy, S. M. & Timms, N. E. Evolution of zircon deformation mechanisms in a
497 shear zone (Lanzo massif, Western-Alps). *Lithos*(0).
498 Kassner, M. E. & Hayes, T. A. 2003. Creep cavitation in metals. *International Journal of Plasticity*
499 **19**(10), 1715-1748.
500 Katayama, I. & Maruyama, S. 2009. Inclusion study in zircon from ultrahigh-pressure metamorphic
501 rocks in the Kokchetav massif: an excellent tracer of metamorphic history. *Journal of the*
502 *Geological Society* **166**(4), 783-796.
503 Katayama, I., Ohta, M. & Ogasawara, Y. 2002. Mineral inclusions in zircon from diamond-bearing
504 marble in the Kokchetav massif, northern Kazakhstan. *European Journal of Mineralogy*
505 **14**(6), 1103-1108.
506 Leroux, H., Reimold, W. U., Koeberl, C., Hornemann, U. & Doukhan, J. C. 1999. Experimental
507 shock deformation in zircon: a transmission electron microscopic study. *Earth and*
508 *Planetary Science Letters* **169**(3-4), 291-301.
509 Li, Z. 1994. The silicate melt inclusions of igneous rocks. In: *Fluid inclusions in minerals: Methods*
510 *and applications* (edited by De Vivo, B. & Frezzotti, M. L.). Virginia Tech, Blacksburgh,
511 Virginia, 73-94.
512 Liu, F., Xu, Z. & Xue, H. 2004. Tracing the protolith, UHP metamorphism, and exhumation ages of
513 orthogneiss from the SW Sulu terrane (eastern China): SHRIMP U-Pb dating of mineral
514 inclusion-bearing zircons. *Lithos* **78**(4), 411-429.

515 Lloyd, G. E. 1987. Atomic number and crystallographic contrast images with the SEM: a review of
516 backscattered electron techniques. *Mineralogical Magazine* **51**, 3-19.
517 MacRae, C. M., Wilson, N. C., Johnson, S. A., Phillips, P. L. & Otsuki, M. 2005. Hyperspectral
518 mapping - Combining cathodoluminescence and X-ray collection in an electron microprobe.
519 *Microscopy Research and Technique* **67**(5), 271-277.
520 Mancktelow, N. S., Grujic, D. & Johnson, E. L. 1998. An SEM study of porosity and grain
521 boundary microstructure in quartz mylonites, Simplon Fault Zone, Central Alps.
522 *Contributions to Mineralogy and Petrology* **131**(1), 71-85.
523 Massonne, H.-J. & Nasdala, L. 2003. Characterization of an early metamorphic stage through
524 inclusions in zircon of a diamondiferous quartzofeldspathic rock from the Erzgebirge,
525 Germany. *American Mineralogist* **88**(5-6), 883-889.
526 Menneken, M., Nemchin, A. A., Geisler, T., Pidgeon, R. T. & Wilde, S. A. 2007. Hadean diamonds
527 in zircon from Jack Hills, Western Australia. *Nature* **448**(7156), 917-920.
528 Moser, D. E., Davis, W. J., Reddy, S. M., Flemming, R. L. & Hart, R. J. 2009. Zircon U-Pb strain
529 chronometry reveals deep impact-triggered flow. *Earth and Planetary Science Letters*
530 **277**(1-2), 73-79.
531 Nasdala, L., Hofmeister, W., Harris, J. W. & Glinnemann, J. 2005. Growth zoning and strain
532 patterns inside diamond crystals as revealed by Raman maps. *American Mineralogist* **90**(4),
533 745-748.
534 Nasdala, L., Kronz, A., Wirth, R., Blanc, P., Kennedy, A. K., Seydoux-Guillaume, A. M.,
535 Lengauer, C. L. & Hanchar, J. M. 2002. Annealing radiation damage and the recovery of
536 cathodoluminescence. *Chemical Geology* **191**(1-3), 121-140.
537 Nasdala, L., Zhang, M., Kempe, U., Panczer, G., Gaft, M., Andrut, M. & Plotze, M. 2003.
538 Spectroscopic methods applied to zircon. In: *Reviews in Mineralogy and Geochemistry:*

539 *Zircon* (edited by Hanchar, J. M. & Hoskin, P. W. O.). *Reviews in Mineralogy and*
540 *Geochemistry* **53**. Mineralogical Society of America, 427-467.
541 Nemchin, A., Timms, N. E., Pidgeon, R., Geisler, T., Reddy, S. M. & Meyer, C. 2009. Timing of
542 crystallization of the lunar magma ocean constrained by the oldest zircon. *Nature*
543 *Geoscience* **2**, 133-136.
544 Nemchin, A. A., Whitehouse, M. J., Menneken, M., Geisler, T., Pidgeon, R. T. & Wilde, S. A.
545 2008. A light carbon reservoir recorded in zircon-hosted diamond from the Jack Hills.
546 *Nature* **454**(7200), 92-95.
547 Prior, D. J., Boyle, A. P., Brenker, F., Cheadle, M. C., Day, A., Lopez, G., Peruzzo, L., Potts, G. J.,
548 Reddy, S., Spiess, R., Timms, N. E., Trimby, P., Wheeler, J. & Zetterström, L. 1999. The
549 application of electron backscatter diffraction and orientation contrast imaging in the SEM
550 to textural problems in rocks. *American Mineralogist* **84**(11-12), 1741-1759.
551 Prior, D. J., Wheeler, J., Peruzzo, L., Spiess, R. & Storey, C. 2002. Some garnet microstructures: an
552 illustration of the potential of orientation maps and misorientation analysis in
553 microstructural studies. *Journal of Structural Geology* **24**, 999-1011.
554 Qin, Z. 1992. Disequilibrium partial melting model and its implication for trace elements
555 fractionations during mantle melting. *Earth and Planetary Science Letters* **112**, 75-90.
556 Raj, R. & Ashby, M. F. 1975. Intergranular fracture at elevated temperature. *Acta Metallurgica*
557 **23**(6), 653-666.
558 Reddy, S. M., Timms, N. E. & Eglington, B. M. 2008. Electron backscatter diffraction analysis of
559 zircon: A systematic assessment of match unit characteristics and pattern indexing
560 optimization. *American Mineralogist* **93**, 187-197.
561 Reddy, S. M., Timms, N. E., Hamilton, P. J. & Smyth, H. R. 2009. Deformation-related
562 microstructures in magmatic zircon and implications for diffusion. *Contributions to*
563 *Mineralogy and Petrology* **157**(2), 231-244.

564 Reddy, S. M., Timms, N. E., Pantleon, W. & Trimby, T. 2007. Quantitative characterization of
565 plastic deformation of zircon and geological implications. *Contributions to Mineralogy and*
566 *Petrology* **153**, 625-645.
567 Reddy, S. M., Timms, N. E., Trimby, P., Kinny, P. D., Buchan, C. & Blake, K. 2006. Crystal-
568 plastic deformation of zircon: A defect in the assumption of chemical robustness. *Geology*
569 **34**, 257-260.
570 Remond, G., Cesbron, F., Chapoulie, R., Ohnenstetter, D., Roquescarmes, C. & Schvoerer, M.
571 1992. Cathodoluminescence Applied to the Microcharacterization of Mineral Materials - a
572 Present Status in Experimentation and Interpretation. *Scanning Microscopy* **6**(1), 23-68.
573 Rybacki, E., Wirth, R. & Dresen, G. 2008. High-strain creep of feldspar rocks: Implications for
574 cavitation and ductile failure in the lower crust. *Geophysical Research Letters* **35**, L04304.
575 Smyth, H. R., Hamilton, P. J., Hall, R. & Kinny, P. D. 2007. The deep crust beneath island arcs:
576 Inherited zircons reveal a Gondwana continental fragment beneath East Java, Indonesia.
577 *Earth and Planetary Science Letters* **258**(1-2), 269-282.
578 Stroh, A. N. 1957. A theory of the fracture of metals. *Advances in Physics* **6**, 418-465.
579 Stünitz, H., Fitz Gerald, J. D. & Tullis, J. 2003. Dislocation generation, slip systems, and dynamic
580 recrystallization in experimentally deformed plagioclase single crystals. *Tectonophysics*
581 **372**(3-4), 215-233.
582 Thomas, J. B., Bodnar, R. J., Shimizu, N. & Chesner, C. A. 2003. Melt Inclusions in Zircon.
583 *Reviews in Mineralogy and Geochemistry* **53**(1), 63-87.
584 Thomas, J. B., Bodnar, R. J., Shimizu, N. & Sinha, A. K. 2002. Determination of zircon/melt trace
585 element partition coefficients from SIMS analysis of melt inclusions in zircon. *Geochimica*
586 *et Cosmochimica Acta* **66**(16), 2887-2901.
587 Timms, N., Kinny, P. & Reddy, S. 2006. Enhanced diffusion of Uranium and Thorium linked to
588 crystal plasticity in zircon. *Geochemical Transactions* **7**(1), 10.

589 Timms, N. E., Kinny, P. D., Reddy, S. M., Evans, K., Clark, C. & Healy, D. 2011. Relationship
590 among titanium, rare earth elements, U-Pb ages and deformation microstructures in zircon:
591 Implications for Ti-in-zircon thermometry. *Chemical Geology* **280**(1-2), 33-46.
592 Timms, N. E., Li, J. & Reddy, S. M. 2009. Quantitative microstructural characterization of
593 natrojarosite scale formed during high-pressure acid leaching of lateritic nickel ore.
594 *American Mineralogist* **94**(8-9), 1111-1119.
595 Timms, N. E. & Reddy, S. M. 2009. Response of cathodoluminescence to crystal-plastic
596 deformation in zircon. *Chemical Geology* **261**, 11-23.
597 Timms, N. E., Reddy, S. M., Healy, D., Nemchin, A. A., Grange, M. L., Pidgeon, R. T. & Hart, R.
598 D. in press. Resolution of impact-related microstructures in lunar zircons: A preliminary
599 shock-deformation mechanism map. *Meteoritics and Planetary Science*.
600 Trepmann, C. A. & Stöckhert, B. 2003. Quartz microstructures developed during non-steady state
601 plastic flow at rapidly decaying stress and strain rate. *Journal of Structural Geology* **25**(12),
602 2035-2051.
603 Vernooij, M. G. C., Kunze, K. & den Brok, B. 2006. `Brittle' shear zones in experimentally
604 deformed quartz single crystals. *Journal of Structural Geology* **28**(7), 1292-1306.
605 Weertman, J. 1986. Zener-Stroh crack, Zener-Hollomon parameter, and other topics. *J. Appl. Phys.*
606 **60**(6), 1877-1887.
607 Westwood, C., Pan, J. & Crocombe, A. D. 2004. Nucleation, growth and coalescence of multiple
608 cavities at a grain-boundary. *European Journal of Mechanics - A/Solids* **23**(4), 579-597.
609 Wittmann, A., Kenkmann, T., Schmitt, R. T. & Stöffler, D. 2006. Shock-metamorphosed zircon in
610 terrestrial impact craters. *Meteroics & Planetary Science* **41**(3), 433-454.
611
612
613

614 **Figure Captions**

615 Figure 1. (a) Panchromatic cathodoluminescence image of zircon grain 8 from the deformed
616 magmatic population from sample Jhs2Pon4 showing cores and oscillatory zoned rim. (b)
617 Panchromatic cathodoluminescence image of zircon grain 5.

618

619 Figure 2. (a) Orientation contrast image (OCI) of grain 8 showing deformation microstructure.
620 Horizontal stripes are charging artifacts. (b) Detail of area shown in (a). (c) OCI showing
621 deformation microstructure surrounding pores. White arrows highlight sub-micron (type 2) pores
622 along orientation boundaries. (d) Secondary electron (SE) image of the polished surface (oblique
623 view) of grain 5 showing trails of pores and a magnetite inclusion. The rectangular pit in the
624 foreground has been milled using a focused ion beam to a depth of 6.5 μm. (e) Detailed SE image
625 of the mixed magnetite porosity. The lower half of the image shows a vertical cross section through
626 the irregular shaped pore beneath the sample surface. Dark straight lines on (b) and (c) are surface
627 scratches.

628

629 Figure 3. Pore size distribution. Data represents the maximum diameter of pores measured from an
630 orientation contrast image of an area of grain 8 shown in Fig. 2b.

631

632 Figure 4. (a-b) Orientation maps from electron backscatter diffraction data for grains 8 and 5,
633 respectively. Coloured for cumulative crystallographic misorientation (in degrees) from orientation
634 at a reference point (indicated by red cross). The locations of type 1 pores are indicated by white
635 arrows. The trace of CL zoning is shown by white lines. Horizontal features are artifacts of beam
636 scanning in the SEM. (b) Shows microstructure surrounding a magnetite inclusion. Orientation
637 boundaries are shown as black lines. Inset (i) shows cumulative misorientation (5°) across the
638 magnetite inclusion in (b). Step size for maps is 0.1 μm. (a) contains 233126 data points, (b)

639 contains 98137 data points. (c-d) Pole figures of the low-index crystallographic axes in zircon for
640 every data point shown in maps (a) and (b), respectively. Colour scheme as in (a) and (b). The (001)
641 poles cluster in both (c) and (d), and the domination by one colour is because all axes plot on top of
642 each other in the plot, so are dominated by the last points in the plot sequence. In contrast, the
643 systematic colour dispersion on small circles for all other axes indicates these are all rotated around
644 the c-axis. Pole figures are lower hemisphere, equal area projections.
645
646 Figure 5. (a) and (b) Maps to show the local gradients in crystallographic misorientation within
647 deformed regions around inclusions in grains 8 and 5, respectively. Each pixel is coloured for the
648 mean misorientation with its immediate neighbouring analytical points (i.e., a local 3x3 pixel grid).
649 Units are degrees per 0.3 μm. Subgrain boundaries between adjacent pixels with a crystallographic
650 misorientation greater than 3° are shown as solid maroon lines. Non-indexed points that coincide
651 with pores are shown in green, and other non-indexed points are white. Magnetite inclusion in (b) is
652 shown in blue. (a) and (b) show that the microstructures predominantly consist of low-angle (<10°)
653 subgrain boundaries. Horizontal features in (a) are artifacts of beam scanning in the SEM. (c) and
654 (d) Maps showing >1° subgrain boundaries coloured for misorientation axis direction relative to the
655 sample x-y-z reference frame for grains 8 and 5, respectively. Boundaries are assigned colours
656 based on the scheme shown in the lower hemisphere equal area projection legend such that steeply
657 plunging misorientation axes are blue, and shallowly plunging misorientation axes are
658 red/yellow/green. The mean orientation of the grain is shown by the low-index directions
659 superimposed on the legends. Note: the difference in the colour scheme for (d) is because the map
660 has been rotated 90° from the orientation of data acquisition so that <c> is (sub)parallel to y. (c) and
661 (d) show that *c*-axis-parallel misorientation axes are the most prevalent. (e) and (f) are equal area
662 lower hemisphere projection of misorientation axis trends for 5-15° low-angle boundaries shown in
663 (c) and (d), respectively.

664

665 Figure 6. (a) EBSD map of grain 5 showing the location of FIB-milled TEM foils. (b) SE image of
666 *in situ* region of interest for TEM foil (i) during FIB milling preparation. (c) Thinned TEM foil (i)
667 attached to TEM grid. (d) TEM image from foil (i) of two boundaries with different misorientation
668 axes around <c>. Strain can be seen associated with dislocations in the 1.4° boundary. (e) TEM
669 image of a 4° boundary in foil (i). (f) and (g) images of a boundary in foil (ii). (f) A rare free
670 dislocation (FD) can be seen in the far right. (g) A detail of the area shown by the white box in (f).
671 The boundary plane changes orientation from ~(001) at x to ~(011) at point z and is aligned with
672 the viewing direction at point y. Periodic contrast can be seen along the boundary at ~20 nm
673 spacing. Viewing direction for (f) and (g) is ~5 degrees from [100]. Black spots in TEM images are
674 either nano-scale inclusions, centres of natural radiation damage or artefacts of FIB milling.
675

676 Figure 7. Hyperspectral CL data from a deformed area of grain 8. (a) False colour hyperspectral CL
677 map. Blue, green and red channels assigned to 330-450 nm, 450-500 nm and 500-650 nm ranges,
678 respectively. Colour change from blue-green to yellow-orange indicates a relative increase in CL
679 emission in the 450-650 nm range. Black arrows indicate where low-angle boundaries connect with
680 the zircon grain boundary. (b) Mean CL spectra from whole map and numbered areas shown in (a).
681 Vertical axis shows total signal in arbitrary units (a.u.). (c) CL spectra from (a) normalized to core
682 spectra showing changes in CL emission relative to the core spectra. Vertical axis shows signal
683 relative to that of area 4 shown in (a), in arbitrary units (a.u.). The positions of dominant peaks for
684 CL-active REE in the emission region of interest are labeled. REE peak data from Blanc (2000) and
685 Gaft et al. (2000).
686

687 Figure 8. (a) Conceptual diagram to show the formation of cavities during creep. (i) Formation of
688 cavities along low-angle boundaries (LAB) by Zener-Stroh and vacancy diffusion mechanisms.

689 Dislocations and vacancies migrate into LABs during dislocation creep. (ii) Coalescence of cavities
690 at triple junctions to produce type 2 pores. (b) Diagrams to show the evolution of microstructures
691 around primary (type 1 pores) and mineral inclusions in zircon. (i) Initial state involves strain-free
692 zircon and various inclusions. (ii) Initiation of deformation results in localized lattice strain around
693 inclusions. (iii) As deformation progresses, low-angle boundaries connect in networks, new
694 subgrains form, and pore walls become concave.
695
696

Figure 1

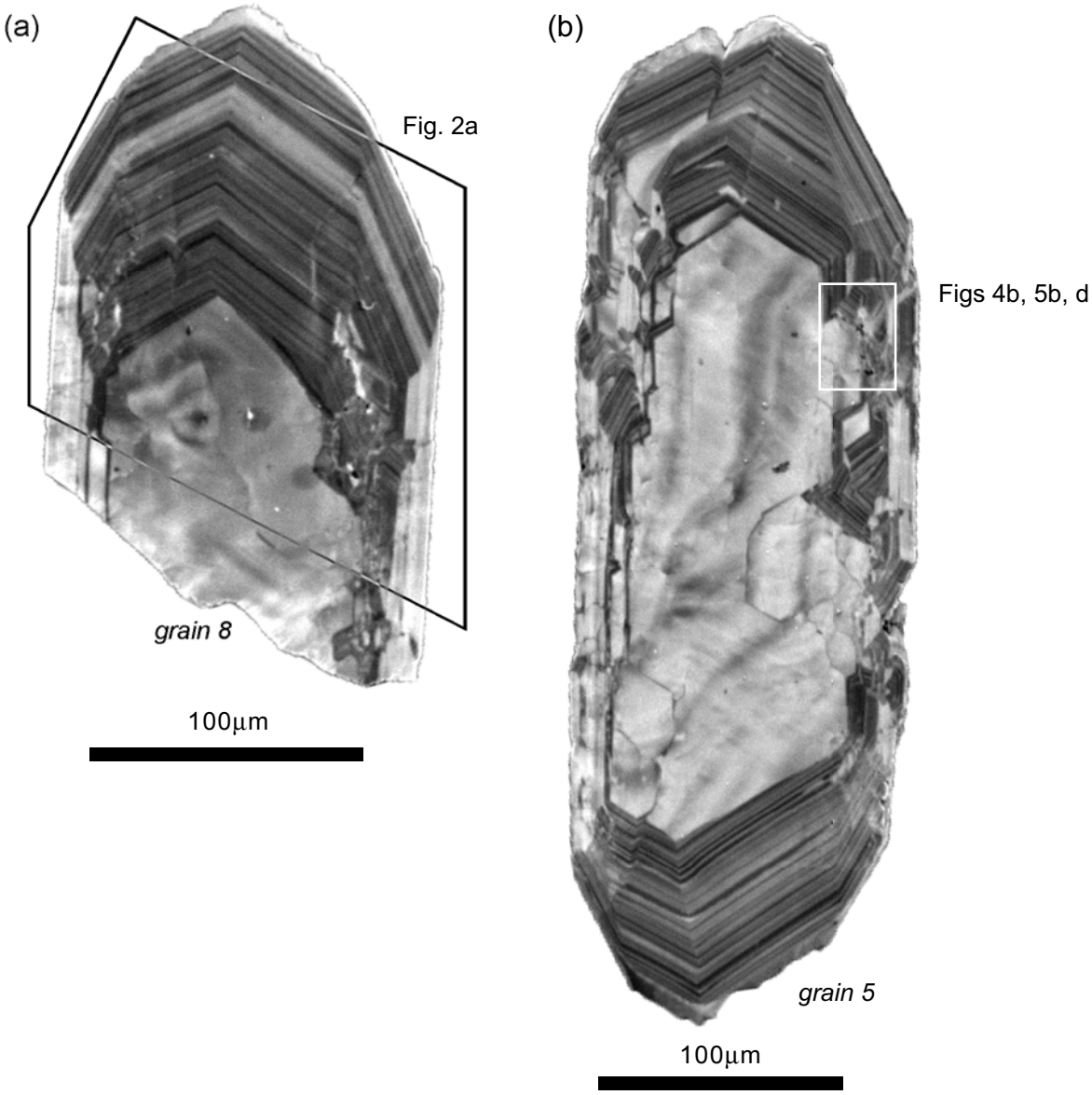

Figure 1

Figure 2

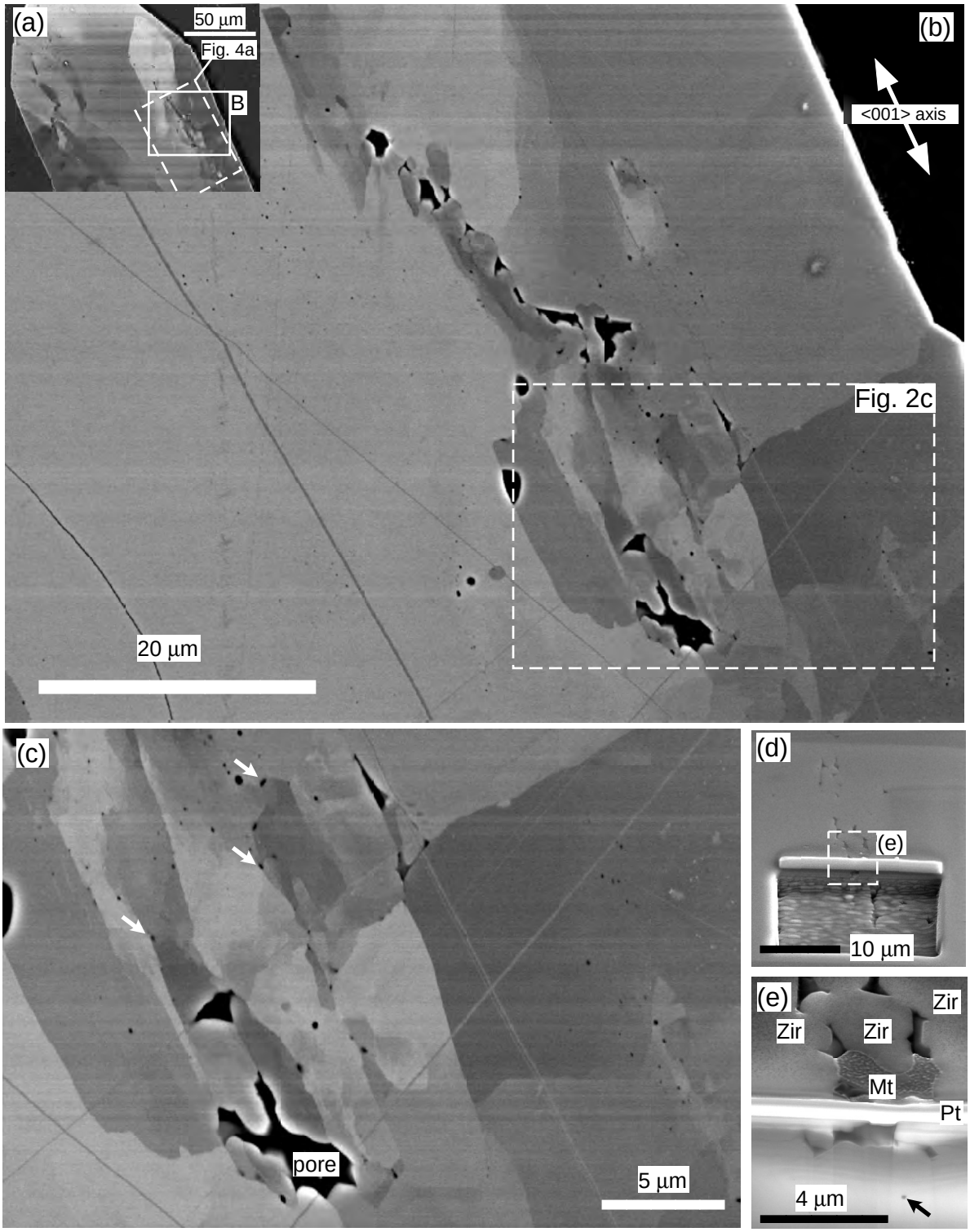

Figure 2

Figure 3

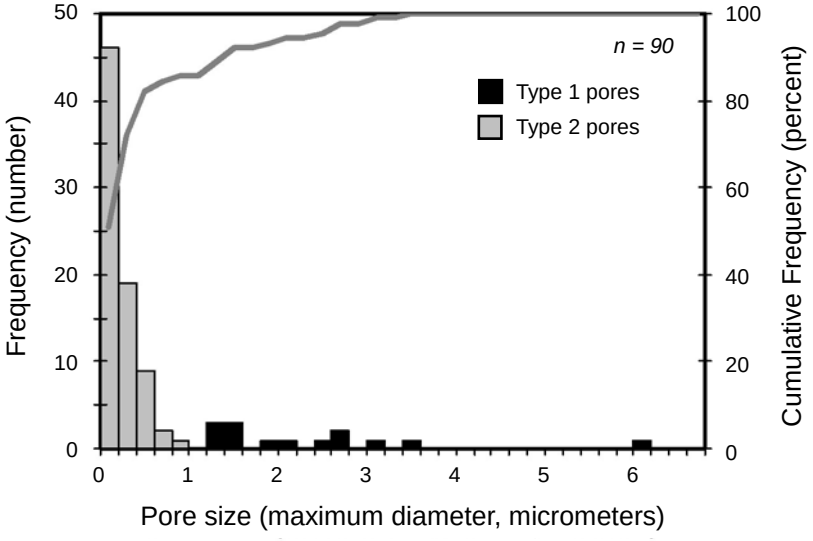

Figure 3

Figure 4

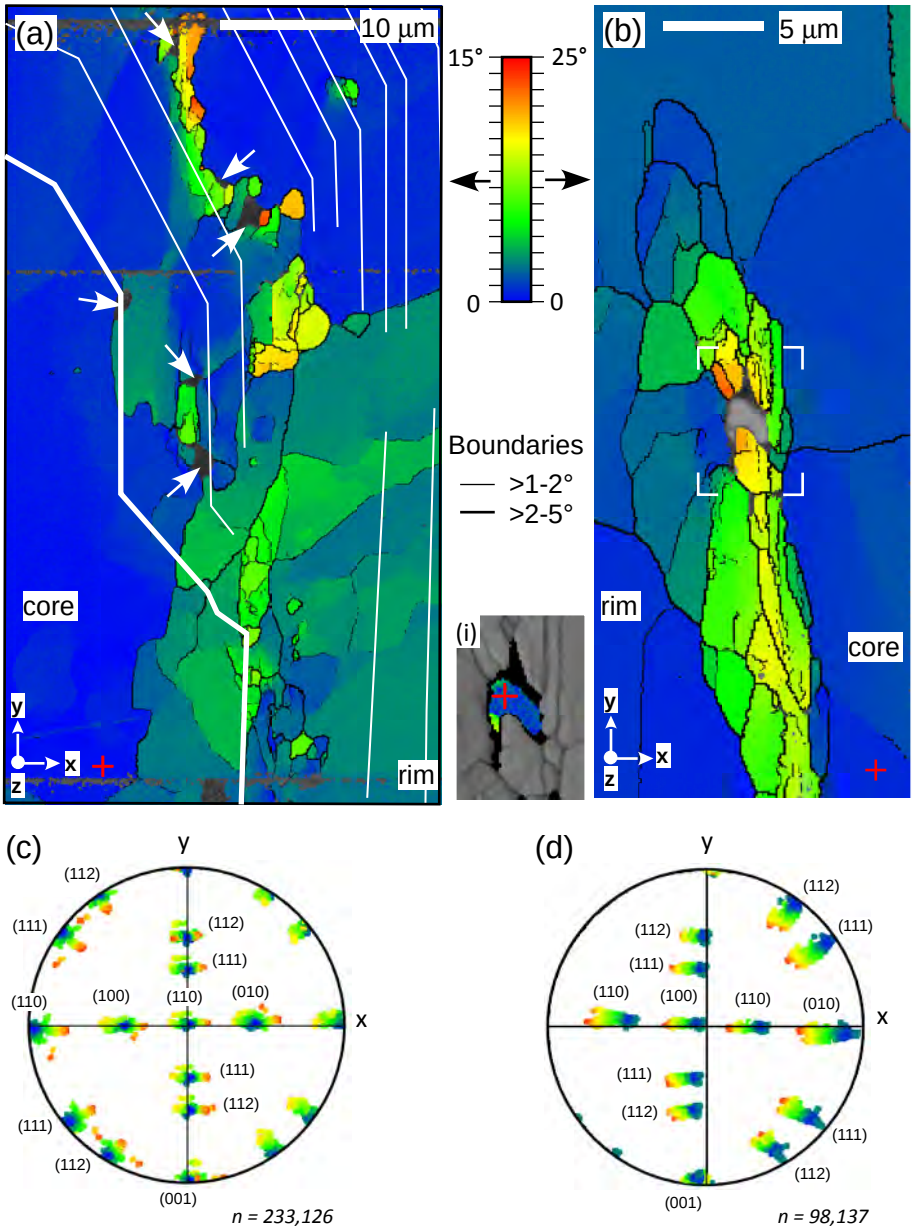

Figure 4

Figure 5

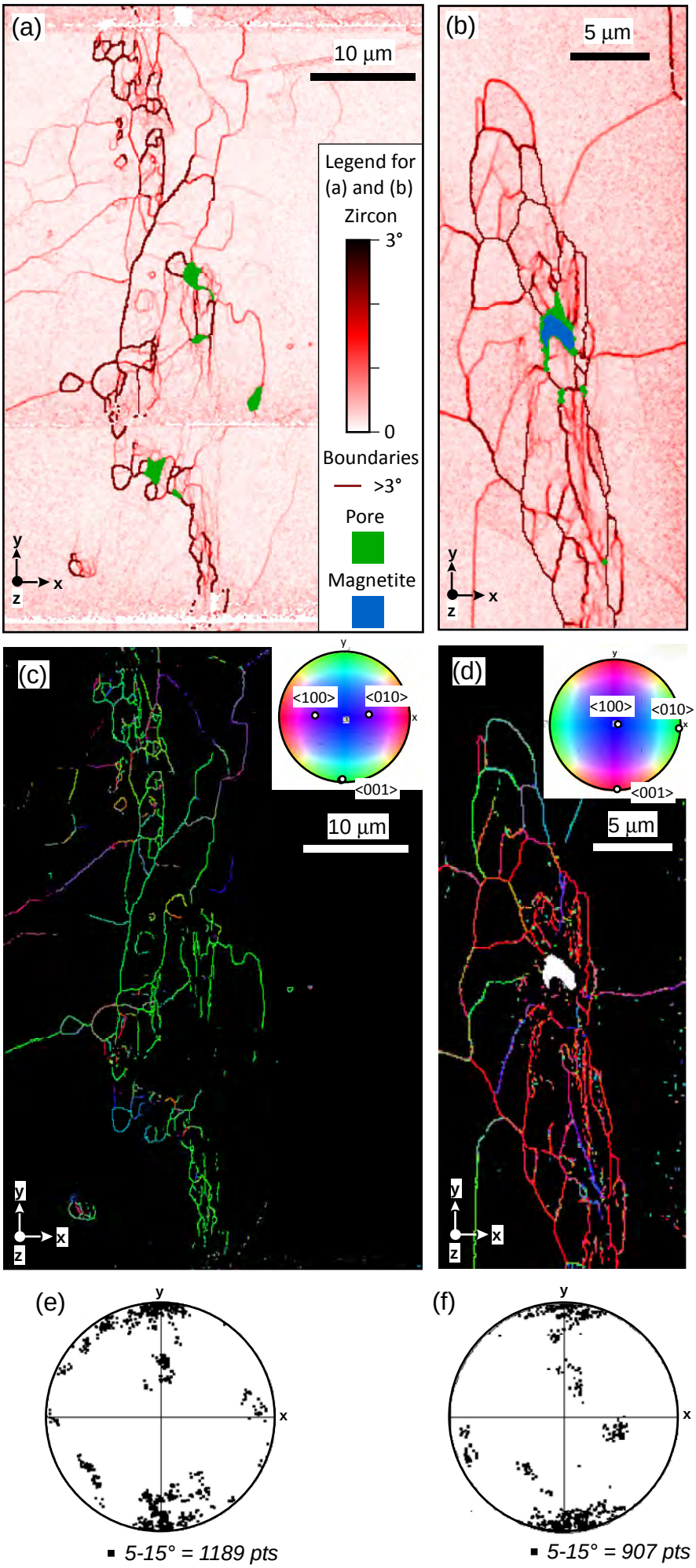

Figure 5

Figure 6

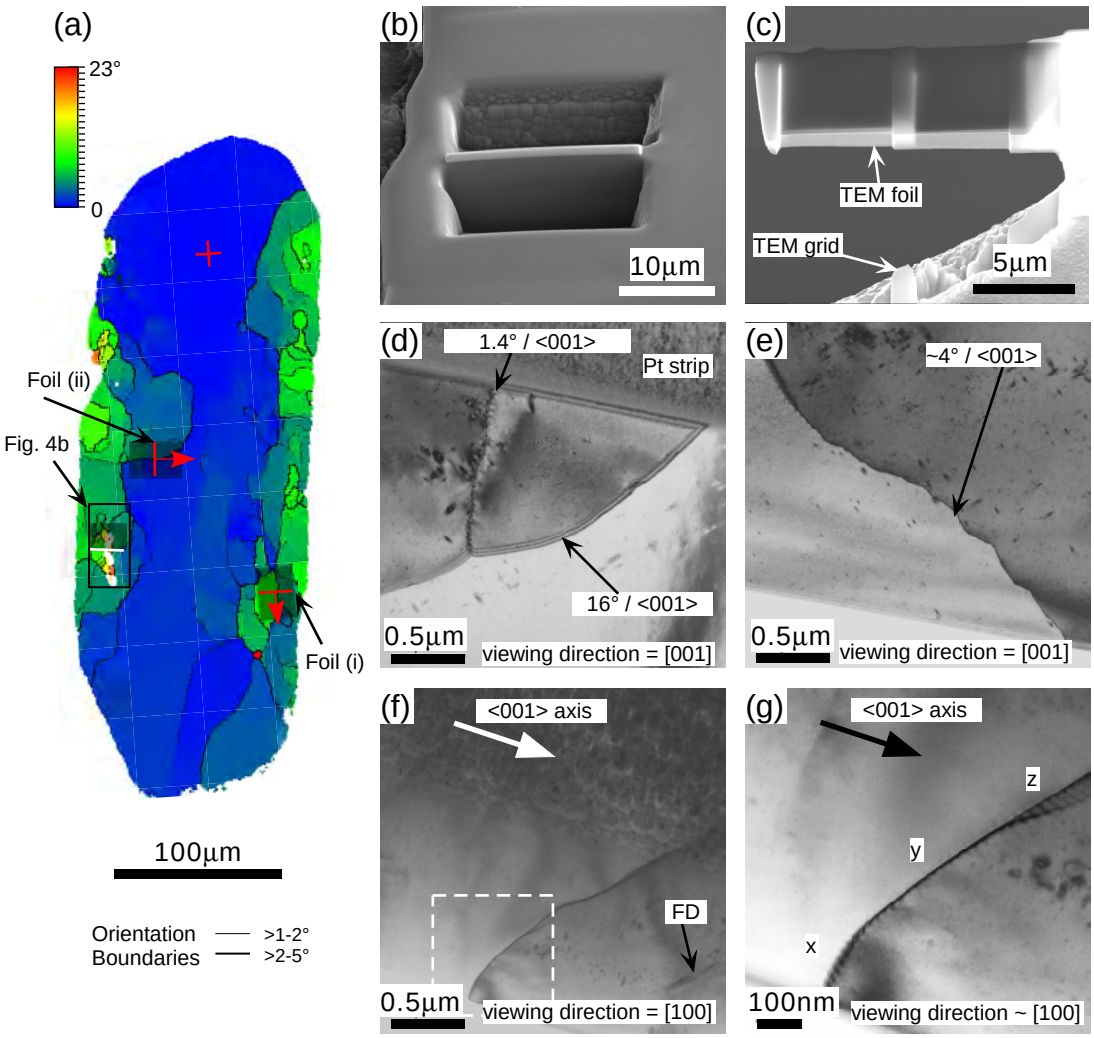

Figure 6

Figure 7

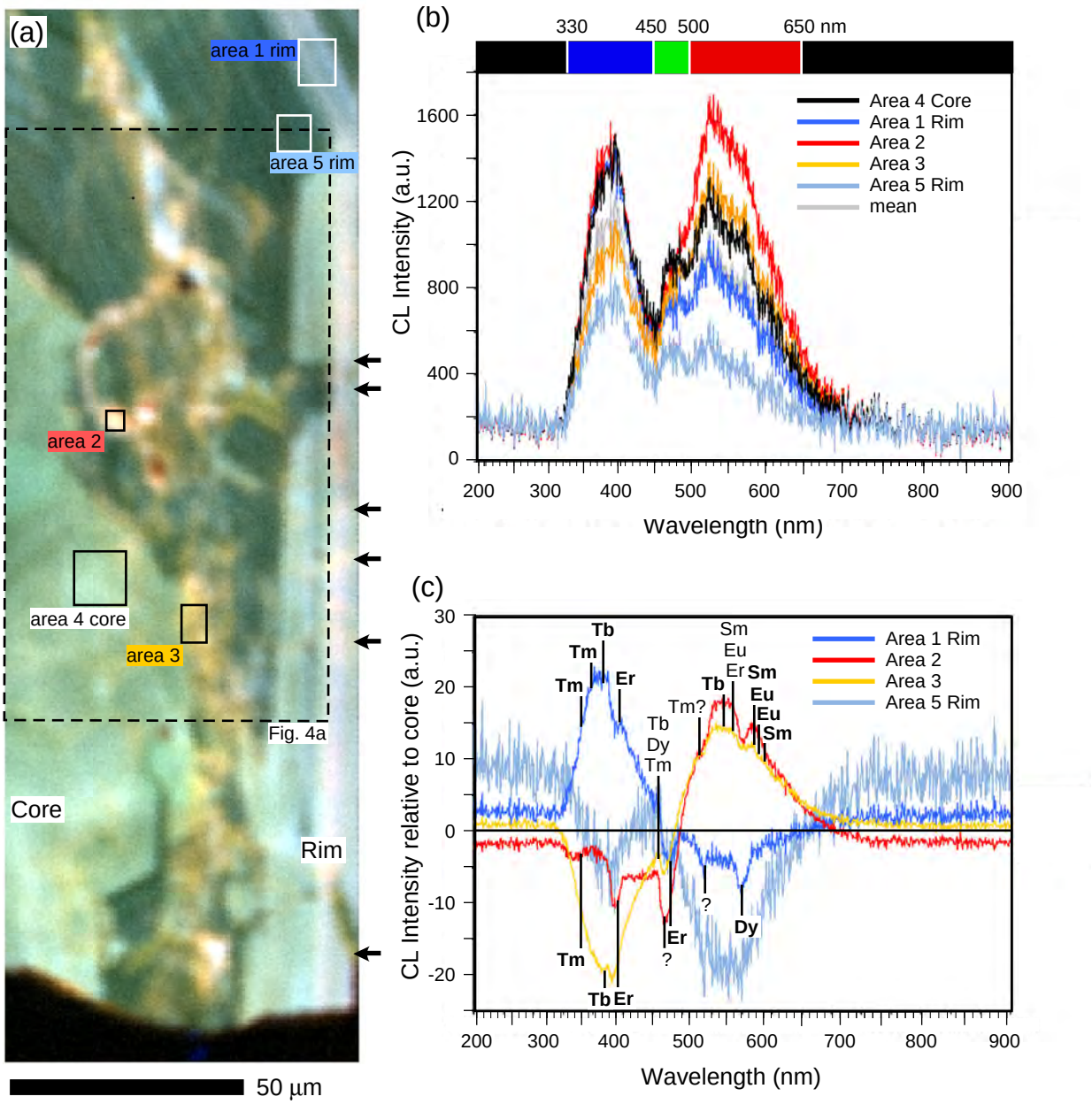

Figure 7

Figure 8

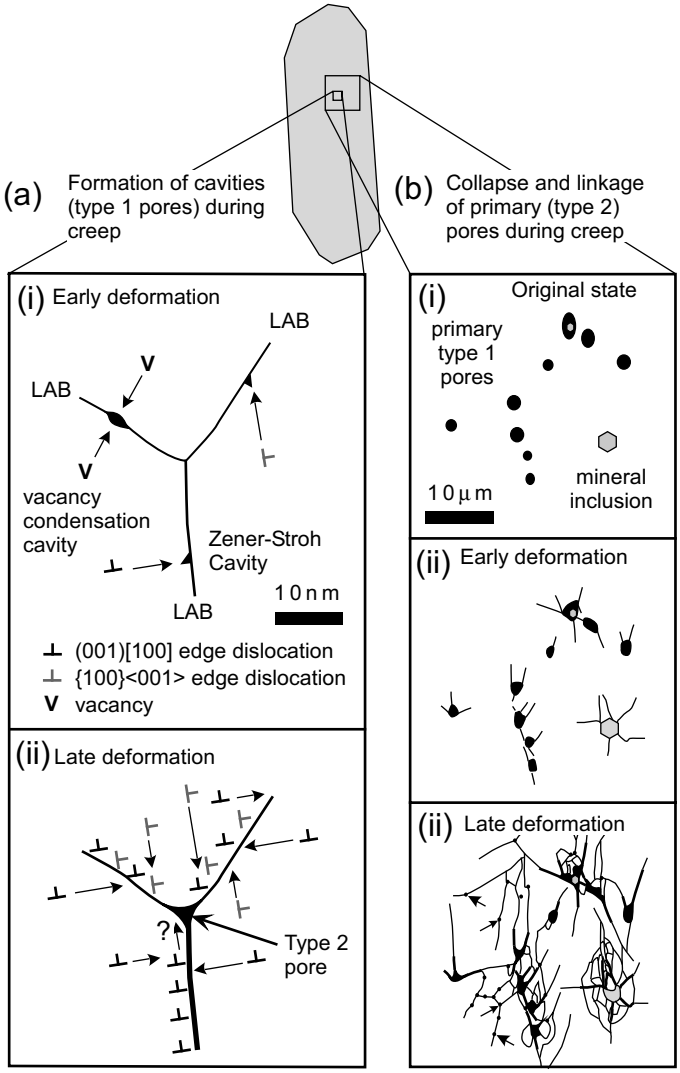

Figure 8

Table 1

Table 1. SEM and EBSD settings and statistics.

Technique	SEM	Detector / Acquisition system	Acc. Voltage (kV)	Probe current	Working Distance (mm)	Tilt (degrees)
PCL	Phillips XL30 (W-filament)	KE Developments	10	Spot 7	17.4	0
OCI	Zeiss Neon Dual FIB-FEG	Annular Backscatter Detector	30	50pA	4.7-5.4	0
EBSD	Phillips XL30 (FEG)	Oxford Instruments Channel 5.9	20	Spot 5	20	70
FIB	Helios D433 Dual FIB-FEG	Helios	5 / 30	16pA to 9.7nA	4.5	52
λCL	JEOL 8530F FEG-EPMA	XCLent III	10	10nA	fixed	0

EBSD Settings	**Fig. 4a, 5a,c**	**Fig. 4b, 5b, d**	**Fig. 6a**
EBSP collection time per frame (ms)	60	60	60
Background (frames)	64	64	64
EBSP noise reduction (frames)	4	4	4
(binning)	4x4	4x4	4x4
(gain)	Low	Low	Low
Hough resolution	65	65	65
Match units	zircon*	zircon*, magnetite	Zircon*
Band detection – No. of bands	8	8	8
Step distance (μm)	0.1	0.1	1
Indexing (percent)	97.14	Zircon: 97.17, Magnetite: 0.46	96
Data noise reduction – 'wildspike' removal	Yes	Yes	Yes
- nearest neighbour zero solution extrapolation	5	5	5

* generated from zircon crystal structure at 9.8 Atm (~1MPa) (Hazen & Finger 1979).